Article:
Palaferri, D, Todorov, Y, Bigioli, A et al. (11 more authors) (2018) Room-temperature nine-μm-wavelength photodetectors and GHz-frequency heterodyne receivers. Nature, 556. pp. 85-88. ISSN 0028-0836

https://doi.org/10.1038/nature25790

Room temperature 9 μm photodetectors and GHz heterodyne receivers

Daniele Palaferri[1], Yanko Todorov[1], Azzurra Bigioli[1], Alireza Mottaghizadeh[1], Djamal Gacemi[1], Allegra Calabrese[1], Angela Vasanelli[1], Lianhe Li[2], A. Giles Davies[2], Edmund H. Linfield[2], Filippos Kapsalidis[3], Mattias Beck[3], Jérôme Faist[3] and Carlo Sirtori[1]

[1] Laboratoire Matériaux et Phénomènes Quantiques, Université Paris Diderot, Sorbonne Paris Cité, CNRS-UMS 7162, 75013 Paris, France
[2] School of Electronic and Electrical Engineering, University of Leeds, Leeds LS2 9JT, United Kingdom
[3] ETH Zurich, Institute of Quantum Electronics, Auguste-Piccard-Hof 1, Zurich 8093, Switzerland

Room temperature operation is mandatory for any optoelectronics technology which aims to provide low-cost compact systems for widespread applications. In recent years, an important technological effort in this direction has been made in bolometric detection for thermal imaging[1], which has delivered relatively high sensitivity and video rate performance (~ 60 Hz). However, room temperature operation is still a major challenge for semiconductor photodetectors in the 8–12 μm wavelength band[2], and all developments for applications such as imaging, environmental remote sensing and laser-based free-space communication[3-5] have therefore had to be realised at low temperatures. For these devices, high sensitivity and high speed have never been compatible with high temperature operation[6,7]. Here, we show that a 9 μm quantum well infrared photodetector[8], implemented in a metamaterial made of subwavelength metallic resonators[9-12], has strongly enhanced performances up to room temperature. This occurs because the photonic collection area is increased with respect to the electrical area for each resonator, thus significantly reducing the dark current of the device[13]. Furthermore, we show that our photonic architecture overcomes intrinsic limitations of the material, such as the drop of the electronic drift velocity with temperature[14,15], which constrains conventional geometries at cryogenic operation[6]. Finally, the reduced physical area of the device and its increased responsivity allows us to take advantage of the intrinsic high frequency response of the quantum detector[7] at room temperature. By beating two quantum cascade lasers[16] we have measured the heterodyne signal at high frequencies, above 4 GHz. These wide band uncooled detectors shall have therefore a significant impact on technologies such as multichannel coherent Gigabit/s data transfer[17] and high precision molecular spectroscopy[18].

An important intrinsic property of inter-subband (ISB) quantum well infrared photodetectors (QWIPs) based on III-V semiconductor materials that has not yet been exploited is the very short lifetime of the excited carriers. The typical lifetime is of the order of few picoseconds[7], which leads to two important consequences: the detector frequency response can reach up to 100 GHz, and the saturation intensity is extremely high (10^7 W/cm^2)[19]. These figures are ideal for a heterodyne detection scheme where a powerful local oscillator (LO) can drive a strong photocurrent, higher than the detector dark current, that can coherently mix with a signal shifted in frequency with respect to the LO. Notably, these unique properties are unobtainable in infrared inter-band detectors based on mercury-cadmium-telluride (MCT) alloys, which have a much longer carrier lifetime and therefore an intrinsic lower speed response[2,20,21]. Yet, the performance of all photonic detectors is limited by the high dark current that originates from thermal emission of electrons from the wells, and rises exponentially with temperature, thus imposing cryogenic operation (~ 80 K) for high sensitivity measurements. Previously, highly doped (~1x10^{12} cm-2)[22], photovoltaic[23] 10 μm QWIPs and QCDs[24] with large number of quantum wells have been observed to operate up to room temperature, but only when illuminated with powerful sources as CO_2 or free electron lasers.

In the present work, we show that this intrinsic limitation in QWIP detectors can be overcome through use of a photonic metamaterial. We are able to calibrate our detector at room temperature using a black body emitting only hundreds of nW, orders of magnitude smaller than that required previously. To date, room temperature performance with values comparable to those that we report here has only been demonstrated in the 3–5 μm wavelength range, using quantum cascade detectors (QCDs)[24-26] and MCT standard detectors[27].

The photonic metamaterial structure is shown in Fig. **1a**. The GaAs/AlGaAs QWIP[8] contains N_{qw} = 5 quantum wells absorbing at 8.9 μm wavelength (139 meV) that has been designed according to an optimized bound-to-continuum structure from ref. **7**. The absorbing region is inserted in an array of double-metal patch resonators[9-12], which provides sub-wavelength electric field confinement and act as antennas. The resonant wavelength is fixed by the patch size s through the expression $\lambda = 2sn_{eff}$, where n_{eff} = 3.3 is the effective index[9]. The structures with s=1.3 μm are thus in close resonance with the peak responsivity of the detector.

In our structure, the microcavity increases the device responsivity by a local field enhancement in the thin semiconductor absorber[10], while the antenna effect extends the photon collection area of the detector, A_{coll}, making it much larger than the electrical area $\sigma = s^2$ of the device[13]. As the detector photocurrent is proportional to A_{coll}, while the dark current is proportional to σ, for the same number of collected photons there is therefore a substantial reduction of the dark current that results in a net increase of the detector operating temperature.

Besides the collection area A_{coll}, which defines the absorption cross section per patch resonator, another crucial parameter is the contrast C of the reflectivity resonance shown in Fig. **1b**. This parameter quantifies the fraction of the incident photon flux absorbed collectively by the array. As shown in Fig. **1c**, the contrast can be adjusted by changing the array periodicity p[10]. Optimal detector responsivity is obtained at the *critical coupling point*, $C = 1$, where all incident radiation is coupled into the array. The collection area per patch is related to the contrast according to the expression $A_{coll} = Cp^2\xi$, where the factor $\xi = 0.7$ takes into account the polarizing effect of the connecting wires (Methods)[13]. From the data in Fig. **1c**, the critical coupling is obtained with a period $p = 3.3$ µm, which corresponds to a collection area $A_{coll} = 7.5$ µm², four times larger than the electrical area $\sigma = 1.7$ µm² of the patch.

The device processing has been optimized in order to generate current solely under the metallic square patches and not below the 150 nm wide leads connecting them. To this end we have realised ohmic contacts between the patches and the underlying semiconductor layers using PdGeTiAu annealed alloy, while a Schottky barrier, made by depositing TiAu, prevents vertical current between the metallic wire and the semiconductor. Moreover, all cavities are connected to an external wire-bonding pad insulated by an 800-nm-thick Si_3N_4 layer (Methods). Thanks to all these precautions the conductive area is reduced to the sum of the areas of all the patch resonators, which prevents additional dark current from flowing across the device.

In order to quantify the detector performance, we have compared the detector array with a reference device, here referred to as “mesa”, where the same absorbing region is processed into 200 µm diameter circular mesa and light is coupled in through the 45°-polished substrate edge[7]. The mesa reference provides the intrinsic photo-response of the detector (Methods). In Fig. **2a** we compare the peak responsivities for the two configurations, obtained with a calibrated black body source at 1000°C (Methods). The mesa device could be characterized only up to 150 K, as the photo-current becomes undetectable at higher temperatures. The array detectors show a seven-fold enhancement of the responsivity at low temperatures. Most remarkably, the responsivity could be characterized up to room temperature, where the measured responsivity (0.2 A/W) is comparable with the best responsivity for the mesa device measured at around 50 K. We were thus able to record photo-current spectra up to room temperature, Fig. **2b**, which is, to our knowledge, the first type of such measurement with a QWIP operating in the 9 µm band using a thermal source.

By quantifying carefully the number of photons absorbed in each geometry (Methods), we were also able to extract the photoconductive gain g for each structure (Fig. **2c**). We recall that the gain provides the number of electrons circulating per photon absorbed in the QWs[7,28], and is an intrinsic property of the absorbing region. All our devices show the same values of the gain as a function of temperature, irrespective of their fabrication geometry, which proves that the

material properties are identical for the two structures. Following Ref.**7**, the photoconductive gain is proportional to the electron drift velocity in the AlGaAs barriers and its temperature dependence is linked to microscopic scattering processes in polar materials[14,15]. Our results fit well the temperature dependence of the drift velocity described on ref. **14**. The derived low temperature value of the drift velocity is of the order of 6×10^6 cm/s as expected at an electric field of 20 kV/cm for an Al concentration in the range 20–30%[29]. These results account for the temperature drop of the responsivity observed in Fig. **2a**. Above 200 K, the gain acquires an almost constant value g = 0.25 – 0.2, of the order of $1/N_{qw}$. This implies that photoexcited electrons can only *travel* from one well to the next adjacent well, as the mean free path of the electrons is now shorter than the distance between two wells. Very interestingly, in this limit, it clearly appears that a detector based on a single quantum well would be advantageous at high temperatures. These results illustrate how our devices give access to the high temperature physics of quantum detectors, a unique regime unexplored so far.

The best assessment of detector performance is the specific detectivity[7] $D^* = \frac{R\sqrt{A_{det}}}{\sqrt{4egI}}$ plotted in Fig. **3a** for the mesa reference and for the patch devices. The experimental results are compared with our model that describes the impact of the photonic design on the detectivity as a function of the temperature[13]. For clarity, in Fig. **3b** we provide the ratio between the detectivities. At low temperature, we observe an enhancement of only a factor of two. Here, the dark current is negligible and the main source of noise is the background photocurrent induced by the 300 K black body of the environment. In this regime higher responsivity means also higher background noise, and the detectivity enhancement scales with the square root of the responsivities ratio i.e. $(R_{array}/R_{mesa})^{1/2}$= 2.6. The situation is totally different at high temperature, where the dark current is the dominant contribution to the noise. In this case the detectivity enhancement is

$$R_{array}/R_{mesa}\,(A_{coll}/\sigma)^{1/2} \sim 14, \quad (1)$$

and the actual performance of the arrays at 300 K is equivalent to the performance of the mesa reference at 150 K, doubling the temperature of operation. This is a significant improvement, well beyond that is predictable from the low temperature operation. Our device concept therefore takes advantage of both the responsivity enhancement and the strong suppression of the dark current owing to the antenna effect, as expressed by the factor $(A_{coll}/\sigma)^{1/2}$. As explained in Ref. **13**, the combination of the microcavity and the antenna effect thus slows down the decrease of the detectivity with temperature, pushing the detector operation to much higher temperatures than expected.

By exploiting our photonic concepts we have achieved high temperature operation with relative high sensitivities. We now seek to benefit from the inherent very high frequency response together with the reduced electrical capacitance of our devices in order to use them as

heterodyne receivers. In this case, by increasing the power of the local oscillator one may achieve the ultimate heterodyne sensitivity set only by the detector absorption coefficient.

This realization is depicted in Fig. **4a**, where we show schematically the heterodyne arrangement that we used to probe our detector at room temperature. It consists of two single mode distributed feedback (DFB) quantum cascade lasers (QCLs)[16] operating at λ = 8.36 μm. The lasers, used respectively as signal and local oscillator are made collinear by a beam splitter (BS) before they impinge on the detector. The latter is connected via wire bonding to a high frequency coaxial cable that is connected to a spectrum analyser. Each laser has a linewidth of the order of one MHz when current and temperature are stabilised. By adjusting the temperature of each laser, their frequencies are tuned within few GHz (Methods).

When the detector is illuminated by both lasers a clear heterodyne signal appears on the spectrum analyser. In Fig. **4a** we show a measurement at 1.06 GHz, with a 40 dB signal-to-noise ratio. We have measured heterodyne signals up to 4.2 GHz as it is illustrated in Fig. **4b**. Our bandwidth is presently limited by a strong impendence mismatch between the detector and the external circuit. In Fig. **4c** we report the characterisation of the sensitivity of the heterodyne receiver at room temperature. The blue dots correspond to the direct current (DC) saturation curve for the LO, while the red curve is the heterodyne signal at 1 GHz as a function of the signal power. The straight line is a linear fit for the LO saturation curve. The saturation experiment shows that the detector responds linearly up to 78 mW (~ 3.1 kW/cm^2) of incident power. Moreover, the linear fit intercepts the 1 Hz integration band for a power of ~ 0.5 nW, in very good agreement with the measured room temperature detectivity from Fig. **3a**. As can be observed from Fig. **4c**, the heterodyne data are very well fitted with a square root dependence (dashed line) and can reach a signal-to-noise ratio of unity for an incident power of a few pW and an integration time of the order of 10 ms. This clearly shows the strength of the heterodyne technique that let us envision sensitivity in the thermal region at λ = 9 μm which is unreachable with any other technique at room temperature. Note that in our experiment the photocurrent induced by the LO, I_{LO} ~ 0.5 mA is still dominated by the detector dark current , I_{dark} ~ 3.5 mA. By increasing the LO power and/or decreasing the temperature of the detector by few tens of degrees using thermo-cooled elements, these detectors could reach the ultimate heterodyne detection limit, set by their absorption efficiency[7,13] and the relative intensity noise of the local oscillator[30].

In conclusion, we have demonstrated metamaterial photonic detectors operating room temperature with high sensitivity in the second atmospheric window at λ ~ 9 μm. While our detectors show lower DC detectivity than microbolometers, they have an extremely fast frequency response of tens of GHz. Using a quantum cascade laser as a local oscillator, we have implemented a heterodyne detection setup, and validated that these uncooled detectors

can operate as coherent heterodyne receivers up to 4.2 GHz. The heterodyne scheme has, indeed, a tremendous potential for sensitive detection in the mid-(far-) infrared that may outperform all others competing technologies. The combination of high sensitivity with high frequency response (tens of GHz) is the essence of this new class of metamaterial detectors. Nonetheless, we recall that when installed on Peltier elements, the DC detectivity of our devices is comparable to that of uncooled microbolometers.

Our devices will be of extreme relevance for the detection of coherent signals (lasers), in particular for free space high-data-rate transfer[17] and dual comb spectroscopy[31], which is an emerging high resolution spectroscopic technique, for which high speed detectors are essential. In general, well-established applications such as optical free space communications, thermal imaging and environmental remote sensing will greatly benefit from our coherent sensitive detection. Moreover, our estimates show that the heterodyne scheme could also serve for the generation and synthesis of microwaves (up to few hundreds GHz) with quite good efficiency of the order of few percent. Finally, we point out that these coherent detectors are ideally suited to be implemented into photonic integrated circuits (PIC's) where the local oscillator is combined with the heterodyne receiver.

References

1. Wood, R. A. Uncooled microbolometer infrared sensor arrays. In *Infrared detectors and emitters: materials and devices* **8** 149-175, edited by Springer, Boston https://doi.org/10.1007/978-1-4615-1607-1_6 (2001)

2. Rogalski, A. Infrared detectors: status and trends. *Progress in quantum electronics* **27.2**, 59-210 http://dx.doi.org/10.1016/S0079-6727(02)00024-1 (2003)

3. Gunapala, S. D. & Bandara, S. V. in Intersubband Transition in Quantum Wells: Physics and Device Applications I, *Semiconductors and Semimetals* **62**(4) 197–282, edited by H. C. Liu and F. Capasso Academic Press, San Diego (2000)

4. Mizaikoff, B. Peer reviewed: Mid-ir fiber-optic sensors *Am. Chem. Soc.* **75** 258A http://pubs.acs.org/doi/pdf/10.1021/ac031340g (2003)

5. Martini, R., & E. A. Whittaker. Quantum cascade laser-based free space optical communications. *Journal of Optical and Fiber Communications Reports* **2**(4) 279-292 http://dx.doi.org/10.1007/s10297-005-0052-2 (2005)

6. Henini, M. & Razeghi, M. *Handbook of infrared detection technologies* Elsevier, Oxford (2002)

7. Schneider, H. & Liu, H.C. *Quantum Well Infrared Photodetectors Physics and Applications*, Springer, New York United States (2007)

8. Levine, B. F., Choi, K. K., Bethea, C. G., Walker, J., & Malik, R. J. New 10 μm infrared detector using intersubband absorption in resonant tunneling GaAlAs superlattices. *Appl. Phys. Lett.* **50**(16) 1092-1094 http://dx.doi.org/10.1063/1.97928 (1987)

9. Todorov, Y. *et al.* Optical properties of metal-dielectric-metal microcavities in the THz frequency range *Opt. Express* **18** 13886 https://doi.org/10.1364/OE.18.013886 (2010)

10. Feuillet-Palma, C., Todorov, Y., Vasanelli, A., & Sirtori, C. Strong near field enhancement in THz nano-antenna arrays. *Sci. Rep.* **3** 1361 https://doi.org/10.1038/srep01361 (2013).

11. Nga Chen, Y. *et al.* Antenna-coupled microcavities for enhanced infrared photo-detection. *Appl. Phys. Lett.* 104 031113 http://dx.doi.org/10.1063/1.4862750 (2014)

12. Palaferri, D. *et al.* Patch antenna terahertz photodetectors. *Appl. Phys. Lett.* **106** 161102 http://dx.doi.org/10.1063/1.4918983 (2015)

13. Palaferri, D. *et al.* Ultra-subwavelength resonators for high temperature high performance quantum detectors. *New J. Phys.* **18**(11) 113016 http://dx.doi.org/10.1088/1367-2630/18/11/113016 (2016)

14. Grundmann, M. *Physics of Semiconductors* **11** Springer Berlin (2010).

15. Howarth, D. J., & Sondheimer, E. H. The theory of electronic conduction in polar semi-conductors. *Proc. R. Soc. A*: *Mathematical, Physical and Engineering Sciences* **219**(1136) 53-74 http://dx.doi.org/10.1098/rspa.1953.0130 (1953)

16. Faist, J. *et al.* Distributed feedback quantum cascade lasers. *Appl. Phys. Lett.* **70**(20) 2670-2672 http://dx.doi.org/10.1063/1.119208 (1997)

17. Corrigan, P., Martini, R., Whittaker, E. A., & Bethea, C. Quantum cascade lasers and the Kruse model in free space optical communication. *Opt. Express*, 17(6), 4355-4359 https://doi.org/10.1364/OE.17.004355 (2009)

18. Argence, B. *et al.* Quantum cascade laser frequency stabilization at the sub-Hz level. *Nat. Photonics*, 9(7), 456-460 http://doi.org/10.1038/nphoton.2015.93 (2015)

19. Vodopyanov, K. L., Chazapis, V., Phillips, C. C., Sung, B., & Harris Jr, J. S. Intersubband absorption saturation study of narrow III-V multiple quantum wells in the spectral range *Semicond. Sci. Technol.* **12**(6) 708 https://doi.org/10.1088/0268-1242/12/6/011 (1997)

20. Theocharous, E., Ishii, J. & Fox, N. P. A comparison of the performance of a photovoltaic HgCdTe detector with that of large area single pixel QWIPs for infrared radiometric applications *Infrared physics & technology* **46**(4) 309-322. http://doi.org/10.1016/j.infrared.2004.05.002 (2005)

21. Stangier, T., Sonnabend, G., & Sornig, M. Compact Setup of a Tunable Heterodyne Spectrometer for Infrared Observations of Atmospheric Trace-Gases. *Remote Sensing*, 5(7), 3397-3414 (2013)

22. Grant, P. D., Dudek, R., Buchanan, M., & Liu, H. C. Room-temperature heterodyne detection up to 110 GHz with a quantum-well infrared photodetector. *IEEE Photon. Technol. Lett.* **18**(21) 2218-2220 https://doi.org/10.1109/LPT.2006.884267 (2006)

23. Schneider, H., Schönbein, C., Bihlmann, G., Van Son, P., & Sigg, H. High-speed infrared detection by uncooled photovoltaic quantum well infrared photodetectors. *Appl. Phys. Lett.* **70**(12), 1602-1604 (1997)

24. Graf, M., Hoyler, N., Giovannini, M., Faist, J., & Hofstetter, D. InP-based quantum cascade detectors in the mid-infrared. *Appl. Phys. Lett. 88*(24), 241118 http://dx.doi.org/10.1063/1.2210088 (2006)

25. Hofstetter, D. *et al.* Mid-infrared quantum cascade detectors for applications in spectroscopy and pyrometry. *Appl. Phys. B* **100**(2) 313-320 http://dx.doi.org/10.1007/s00340-010-3965-2 (2010)

26. Hinds, S. *et al.* Near-Room-Temperature Mid-Infrared Quantum Well Photodetector. *Adv. Mater.* **23**(46) 5536-5539 http://dx.doi.org/10.1002/adma.201103372 (2011)

27. Piotrowski, J., Galus, W., & Grudzien, M. Near room-temperature IR photo-detectors. *Infrared Physics* **31**(1) 1-48 https://doi.org/10.1016/0020-0891(91)90037-G (1991)

28. Liu, H.C. Photoconductive gain mechanism of quantum-well intersubband infrared detectors *Appl. Phys. Lett.* **60** 1507 http://dx.doi.org/10.1063/1.107286 (1992)

29. Hava, S., & Auslender, M. Velocity-field relation in GaAlAs versus alloy composition. *J. Appl. Phys.* **73**(11) 7431-7434 http://dx.doi.org/10.1063/1.353985 (1993)

30. Gensty, T., Elsäßer, W., & Mann, C. Intensity noise properties of quantum cascade lasers. Opt. Express **13**(6) 2032-2039 https://doi.org/10.1364/OPEX.13.002032 (2005)

31. Villares, G., Hugi, A., Blaser S. & Faist, J. Dual-comb spectroscopy based on quantum-cascade-laser frequency combs, *Nat. Commun.* **5**, 5192 http://dx.doi.org/10.1038/ncomms6192 (2014)

Acknowledgements

We acknowledge financial support from the FP7 ITN NOTEDEV project (Grant. No. 607521), the ERC grant "ADEQUATE", the French National Research Agency (ANR-16-CE24-0020 Project "hoUDINi"), and the EPSRC (UK) projects "COTS" and "HYPERTERAHERTZ" (EP/J017671/1, EP/P021859/1). EHL and AGD acknowledge the Royal Society and the Wolfson Foundation, and thank Dr L. Chen for skilled support with the device processing.

Author contributions

D.P., Y.T. and C.S. conceived the experiments, designed the QWIP structure, analysed the data and wrote the manuscript. D.P. fabricated the QWIP devices and performed measurements and data analysis together with A.B. A.M. and D.G. helped with the heterodyne measurements. A.C. calibrated the blackbody for the responsivity measurements and helped with the characterization of the mesa device. A.V. helped with data analysis. L.L., A.G.D. and E.H.L. grew the QWIP structure and provided the wafer-bonding for the double-metal processing. F.K., M.B. and J.F. provided the DFB QCLs for the heterodyne experiment. All the work has been realised under the supervision of C.S.

Author information

The authors declare no competing financial interests.
Correspondence and requests for materials should be addressed to carlo.sirtori@univ-paris-diderot.fr .

Figure 1|Device concept. Double-metal patch antenna, with the various metallic layers employed for electrical contacts (Methods). The absorbing region contains a QWIP structure (386 nm) with five QWs Si-doped at n=7×10^{11} cm^{-2}.For this metamaterial structure the photon collection area, A_{coll}, is much larger than the electrical area σ. The scale bar on the image is 500 nm. **b**, Reflectivity spectrum (blue curve) of a patch antenna array with s=1.30 μm and a period p=3.30 μm. The dashed line is a Lorentzian fit providing the absorption contrast C. **c**, Contrast C and collection area A_{coll} as a function of the array unit cell area Σ=p^2. The observed saturation of A_{coll} is in agreement with theoretical predictions[13].

Figure 2|Detector characterizations. a, Peak responsivity, measured with a calibrated 1000° C blackbody source, of QWIP devices fabricated in 200 μm diameter mesa (circles), and into patch resonator arrays with s=1.35 μm (squares) and s=1.30 μm (triangles). **b**, Normalized photocurrent spectra of the s=1.30 μm array at 78 K, 200 K and 295 K. **c**, Photoconductive gain and electronic drift velocity of the three devices presented in **2a** as a function of temperature, for 0.5 V bias voltage (21 kV/cm electric field). The drift velocity is obtained using a QW capture time of 5 ps (see ref. **7** and Methods).

Figure 3| Detectivity as a function of the temperature. a, Specific detectivity (2π field of view) as a function of the temperature and at a bias of 0.5 V, for the reference mesa (circles) and two arrays structures: s=1.30 μm (triangles) and s=1.35 μm (squares). The red line is a fit of the reference using $d(T)=d_0/[1+d_1 T\exp(-E_{act}/k_B T)]^{1/2}$ where d_0 and d_1 are fit parameters, E_{act} = 120 meV is the activation energy and k_B is the Boltzmann constant. The blue curve is the model of quantum detectors embedded in patch resonators described in ref. **13**. **b**, Ratio between the detectivities in the two different detector geometries. Dots show the corresponding BLIP temperatures: T_{BLIP}^{mesa} =70 K (mesa) and T_{BLIP}^{cavity} =83 K (patch cavity arrays).

Figure 4|Tunable heterodyne experiment and results. a, Heterodyne arrangement involving DFB QCLs and a cavity array QWIP at room temperature . A 40 dB heterodyne power spectrum is shown, acquired using a spectrum analyser with 1 MHz resolution bandwidth. **b**, Normalized heterodyne power signal (in linear scale).. **c**, Log-log plot of the signal-to-noise ratio as a function of the signal QCL power, for LO power of 40 mW. The noise of the QWIP is calculated using the measured gain and dark current values at room temperature.

Methods

QWIP fabrication. The QWIP structure is grown by MBE (molecular beam epitaxy). It consists of five GaAs quantum wells (QWs), each with a thickness L_{QW} = 5.2 nm and each *n*-doped across the central 4 nm region with Si at a density of N_d = 1.75x10^{18} cm^{-3}, providing a sheet density of n=7×10^{11} cm^{-2} The QWs are separated by $Al_{25}Ga_{75}As$ barriers of thickness L_b = 35 nm. At the top and bottom of this periodic structure GaAs contact layers are grown, with thicknesses $L_{c,top}$ = 100.0 nm and $L_{c,bottom}$ = 50.0 nm and doping $N_{d,top}$ = 4.0x10^{18} cm^{-3} and $N_{d,bottom}$ = 3.0x10^{18} cm^{-3}, respectively. The double-metal structures are obtained through wafer-bonding on a GaAs host substrate using 500 nm gold layers, and by selectively etching down to an etch-stop $Al_{65}Ga_{35}As$ layer grown before the bottom contact. As shown in Fig. **1a**, the patch-antennae are connected by 150 nm thin metallic wires which are realized using electron-beam lithography (consecutive alignments allow different metallic alloy contacts). The final structure is obtained by ICP etching of the semiconductor region between the antennae. The Schottky barrier under the thin metallic wires prevents vertical dark current flow between the metal and the semiconductor[32]. The 45° facet substrate-coupled geometry consists of a 200 µm diameter circular mesa, with annealed Pd/Ge/Ti/Au as a top contact and annealed Ni/Ge/Au/Ni/Au as a diffused bottom contact.

Extended Data Fig. 1 shows a scanning electron microscope (SEM) image of the quantum detector device made of our metamaterial photonic concept. The pixel of the device is 50x50 µm^2. The external pad is connected to the array by the 150 nm wires and is insulated from the bottom ground plane by 800 nm thick Si_3N_4 layer. The TiAu pad connects the device to the external circuit by wire bonding.

Reflectivity and photocurrent analysis. Reflectivity spectra and photocurrent spectra were obtained using a Bruker Vertex interferometer. Reflectivity measurements were performed at a 15° incident angle and at room temperature, and the incident light was polarized perpendicular to the 150 nm thin connecting wires For the photocurrent spectra, QWIP devices were mounted in a cryostat with an internal cooled metallic shield and a ZnSe optical window. Photocurrent and responsivity were measured using a blackbody source at 1000 °C, which was calibrated with an MCT detector. The source is focused onto the detector by two gold parabolic mirrors (f/1 and f/3), providing typical field of view of 60°. The photocurrent is measured with a lock-in technique using an optical chopper at 1059 Hz and a shunt resistance connected to the voltage input of a lock-in amplifier Stanford Research SR1830, without using pre-amplifiers.

Light polarization dependence. Our structures support two fundamental modes, TM_{100} and TM_{010}, which are represented in Extended Data Fig. 2a. This figure shows the vertical electric field E_z in the plane of the resonator, obtained through finite elements simulations. The electric

field distribution follows a standing wave pattern, with a node in the center of the square and maxima at the edges. The connecting wires perturb the TM_{010} mode slightly, which results in a lower coupling efficiency for this mode. As a result, the total photoresponse of the antenna-coupled device has a co-sinusoidal dependence with the light polarization of the normally incident wave.

In Extended Data Fig. 2b, we plot the peak value of the photocurrent for a s = 1.30 μm structure as a function of the polarization of a plane wave incident on the array (open circles), with the 90° direction corresponding to the direction of the connecting wires. The angular integral of the cavity photocurrent peak $I_{photo}(\theta)$ plotted in Extended Data Fig. 2b gives a polarization coupling coefficient $\xi_{array} = \int_0^{2\pi} I_{photo}(\theta) d\theta = 71\%$. The contrast value C of the TM_{100} polarized light is obtained from the measurement of Fig. 1b. For comparison, in the same graph we also plot the polarization dependence of the photoresponse measured for the mesa geometry (open squares). Here the 0° direction corresponds to the growth direction of the QWs, and the incident wave propagates normally to the 45° polished facet. This polar plot therefore recovers the inter-subband selection rule, as expected[7].

Definition of the collection area A_{coll}. As all incident radiation that is not absorbed is reflected, the contrast C provides directly the fraction between the incident P_i and absorbed flux P_a for each patch, $C=P_a/P_i$. If we note by the incident photon flux Φ_i, then the power received by each antenna is $P_i = \Phi_i p^2$, and the power absorbed is by definition $P_a = \Phi_i A_{coll}$. Then using $C=P_a/P_i$ we obtain $A_{coll} = Cp^2$; in the main text we also add a corrective factor of ξ_{array}=0.7 owe to the polarizing effect of the wires, as described in the previous paragraph.

Responsivity, gain and specific detectivity In Extended Data Fig. 3a we show the responsivity curves as function of voltage for both the mesa and the patch cavity with s = 1.35 μm. The decrease of the responsivity with temperature is attributed to the thermal dependence of the charge carrier drift velocity and to an increased phonon-electron interaction[14,15] (see Fig. **2c**). Note that QWIP devices show the typical negative differential photoconductivity, identified as the Gunn effect, which consists of a photocurrent decrease as function of voltage at specific critical fields, at which inter-valley electron scattering is induced in GaAs[7].

The responsivities of the mesa can be expressed by considering the voltage dependent photoconductive gain $g(T,V)$ of the detector active region and the peak inter-subband energy E_{21} = 143 meV (taking into account many-body effects) :

$$R_{mesa}(E_{21}, \mathrm{T}, V) = \eta_{isb}(E_{21})\, eg(\mathrm{T}, V)\, t_{GaAs} \xi_{mesa} / E_{21} \qquad (2)$$

where η_{isb}= 5.0% is the absorption coefficient for the five QW system in the 45° facet geometry, e is the electron charge, $t_{GaAs} = 0.67$ is the substrate transmission coefficient at 8.6 μm and ξ_{mesa}= 0.5 is the polarization factor (only one polarization of the incident light is coupled with the 45° facet). Analogously to Eq. (2), we can define[13]:

$$R_{array}(E_{21}, \mathrm{T}, V) = \frac{B_{isb}(E_{21})}{B_{isb}(E_{21})+Q_{ohm}^{-1}+Q_{rad}^{-1}}\, eg(\mathrm{T}, V)\, C\xi_{array}/E_{21} \quad (3)$$

where Q_{ohm} = 4 and Q_{rad} = 22 represent the ohmic and radiative dissipation of the double metal cavity, respectively, obtained by reflectivity measurements. Indeed, the Lorentzian fit of the reflectivity resonance from Fig. 1b in the main text provides the FWHM and the sum $1/Q_{\mathrm{ohm}}+1/Q_{\mathrm{rad}}$, and Q_{rad} is calculated from the analytical expression provided in Ref.**13**.

The dimensionless parameter B_{isb} quantifies the energy dissipation through inter-subband absorption and is expressed by a lorentzian lineshape:

$$B_{isb}(E) = f_w \frac{E_P^2}{4E_{21}} \frac{\hbar\Gamma}{(E-E_{21})^2+\frac{(\hbar\Gamma)^2}{4}} \quad (4)$$

where $f_w = N_{\mathrm{QW}}L_{\mathrm{QW}}/L$=0.067 is the filling factor of the absorbing QWs on the overall thickness, E_{p} = 47.2 meV is the inter-subband plasma energy, and Γ = 15.0 meV is the full-width-at-half-maximum of the mesa photo-response, obtained by a fit to the experimental data. We obtain a similar value B_{isb}=0.07 for the two resonant cavities s = 1.30 μm and s = 1.35 μm. The absorption coefficient in the antenna-coupled QWIPs is described by the branching ratio $\eta_{array} = \frac{B_{isb}}{B_{isb}+Q_{ohm}^{-1}+Q_{rad}^{-1}}$ = 18.9%. Using Eq. (2) and Eq. (3) with the measurement data in Fig. **2a**, we obtain very similar values for the photoconductive gain for the mesa and the array, as shown for the data at 0.5 V (21 kV/cm) in Fig. **2a**. This confirms that the absorbing regions for the two geometries are identical. Furthermore, the data shows an exponential decrease of the gain as a function of temperature. Following Ref. **7** the photoconductive gain can be defined as:

$$g = \frac{\tau_{capt} v_d}{N_{\mathrm{QW}} L_p} \quad (5)$$

where τ_{capt} = 5 ps is the capture time, v_d is the drift velocity, N_{QW} = 5 is the number of quantum wells and L_p = 40.2 nm is the length of a period in the structure. The thermal dependence of the gain is related directly to the drift velocity and therefore to the electron mobility. Following Ref. **14** we can express the temperature dependence as:

$$g(T) = \frac{1}{\frac{1}{g_0}+\frac{B}{\exp\left(\frac{E_{LO}}{k_B T}\right)}+\left(\frac{E_{AC}}{k_B T}\right)^{3/2}} \quad (6)$$

Here E_{LO}=36 meV is the longitudinal optical phonon energy in GaAs, and the fit parameter g_0=1.25±0.03 expresses the value of the gain at equilibrium (without thermal scattering dependence). The second term in the denominator represents the polar optical scattering (see Ref. **15**) where the parameter B=24.4±1.6 is a dimensionless polar constant and the third term represents the deformation potential scattering caused by interaction of carriers with acoustic phonons, with a corresponding parameter E_{AC}=0.07±0.01 meV which characterizes the acoustic deformation potential. Eq. (6) provides very good fits of the experimental data, confirming the model.

The values of photoconductive gain obtained in this way are used to calculate the detectivity as function of applied voltage, at different temperatures, as illustrated in Extended Data Fig. **3b**.

Heterodyne measurement. The two beams from the QCLs are made collinear using f/0.5 germanium lenses and a beam splitter, and then focused onto the detector by a f/1.5 lens and a λ/4 waveplate to avoid optical feedback (Fig. **3a**). The two lasers are DC biased with a voltage supply and are mounted in two Janis cryostats to stabilize their temperatures using liquid nitrogen flow. The QWIP is polarized by a Keythley 2450 sourcemeter and the heterodyne signal is sent to a spectrum analyser Agilent E4407B using a bias tee. In this arrangement the QWIP detector is at room temperature, without using any cooling system. The QC laser used as the LO is kept at a temperature 254 K while the QC laser used for the signal is kept at 293 K. With the temperature stabilized, it is possible to tune the spectral position of the two DFBs by slightly changing the applied DC current, according to the tuning coefficients β_{LO}=378 MHz/mA and β_S=413 MHz/mA (extracted from a linear fit to the emission frequency of the lasers as a function of temperature and bias).

In the case of a high power LO, the NEP of the heterodyne can be written[7] $NEP_{het}=E_{21}/(\eta\tau)$ where η is the absorption coefficient of the QWIP and τ is the integration time (set by the integration bandwidth Δf as $\tau=1/\Delta f$). For our device in the microcavity array we have a theoretical limit of NEP_{het} of less than 1 aW for an integration time τ= 1 s at 300 K. In the experiment shown in Fig. **4**, the signal-to-noise ratio is still mainly limited by the dark current. The square root fit of the signal-to-noise ratio can be extrapolated to 1, which provides NEP_{het} ~ 10 fW for an integration time of 1 s (NEP_{het} ~ 1 pW for an integration time of 10 ms), that is still four orders of magnitude higher than the theoretical limit. These estimations indicate that a high power LO could achieve sensitivities at the single photon level at room temperature.

Linearity and Heterodyne Measurement In Extended Data Fig. 4 we show the spectra of the two QCLs compared to the room temperature response of the QWIP in the microcavity array geometry. We notice that the lasers are detuned from the maximum intersubband absorption, resulting in a detector photoresponse that is half of the maximum achievable. This is an important remark because the responsivity and detectivity values we report in Figs. 2 and 3

correspond to the peak values of detector photoresponse. The background-limited NEP (noise equivalent power) is defined as NEP=$\sqrt{A_{det}}$/D*. The detector area A_{det} corresponds to the 50x50µm² area of the whole array, which is equal to the number of patches N_{patch} multiplied by the array unit cell area $\Sigma=p^2$. Indeed, in the critical coupling point, all incident radiation is absorbed by the array, and therefore the collection area for each patch A_{coll} coincides with the array unit cell $\Sigma=p^2$. Using our measured value of detectivity at 295 K for the cavity with s = 1.30 µm at 0.5 V (Fig. 3) we have $D^*=2.8\times10^7$ cmHz$^{0.5}$/W and NEP = 0.2 nW/Hz$^{0.5}$. Taking into account the 50% spectral overlap, we obtain NEP = 0.4 nW/Hz$^{0.5}$, which agrees with that observed from the linearity measurement in Fig. **4c**. Therefore the data presented in the main text are perfectly consistent.

References:

32. Sze, S.M. and Kwok, Ng. *Physics of semiconductor devices*, Wiley, New Delhi India (2011)

Data availability statement

The authors declare that all data supporting the findings of this study are available within the paper and its supplementary information files.

Extended Data Figure 1|Global view of the device
Scanning electron microscope (SEM) picture of mid-infrared QWIP structure embedded into 50x50 µm² array of patch resonators. We have indicated the top TiAu contact evaporated onto a 800 nm thick Si_3N_4 insulating layer.

Extended Data Figure 2|Polarization dependence of the photo-response
a, Finite element simulation of the E_z field component coupled with the patch cavity QWIP, for the TM_{100} and the TM_{010} modes. **b**, Polar graph of the cavity photocurrent peak as function of the wire grid polarization angle. The photocurrent is normalized at its maximum at 0˚. The open circles are the results for the cavity array, where the 90° direction corresponds to the connecting wires. The open squares are the results for the mesa geometry, where the 0˚ direction corresponds to the growth direction of the QWs.

Extended Data Figure 3|Mesa and cavity array detector characteristics
a, Responsivity of the mesa and the *s*=1.35 µm antenna-coupled devices as function of applied voltage. The temperature in K of the QWIP is indicated for each measured curve. **b**, Specific detectivity for the mesa and the microcavity devices as a function of the applied bias at different temperatures.

Extended Data Figure 4| Spectral characteristics of the two lasers and the QWIP detector
a, Emission spectra of the QC lasers (QCL_{LO} and QCL_S) compared to the room temperature response of the microcavity QWIP. **b**, Blown up version of the spectrum showing the two distinct QCL emission lines. The QCL_{LO} was operated at 330 mA with temperature stabilized at 293 K, and the QCL_S was operated at 280 mA with temperature stabilized at 254 K.

504

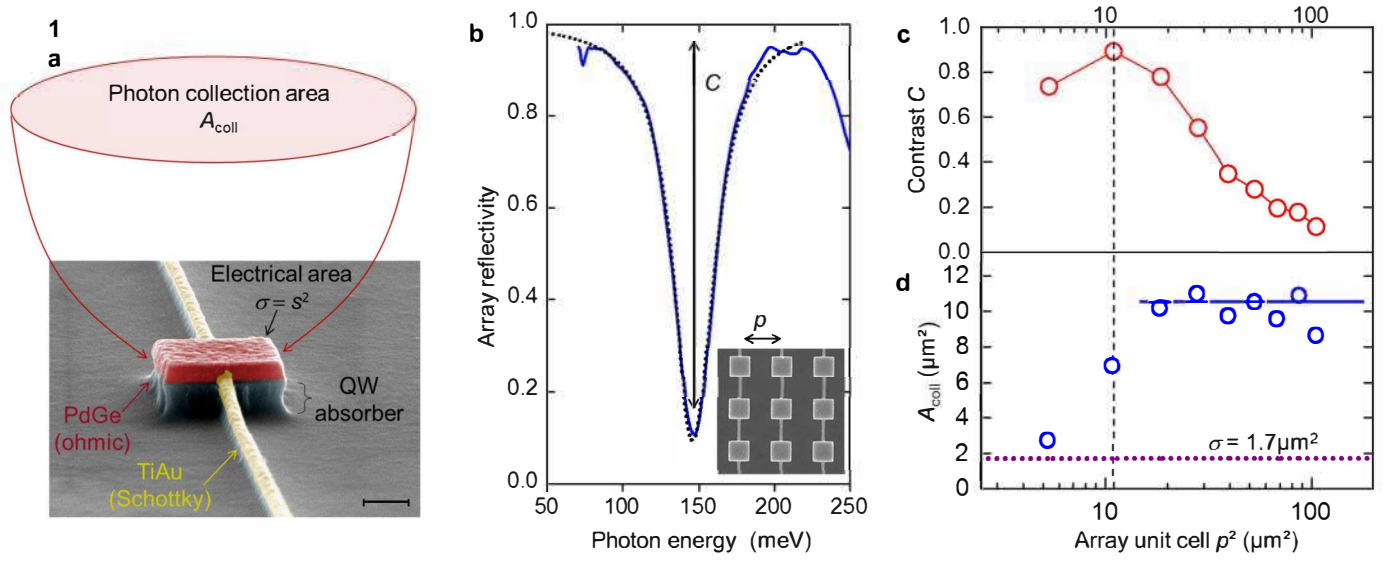
1
a
Photon collection area
A_{coll}
Electrical area
$\sigma = s^2$
QW
absorber
PdGe
(ohmic)
TiAu
(Schottky)
b
Array reflectivity
Photon energy (meV)
C
p
c
Contrast C
d
A_{coll} (μm²)
σ = 1.7μm²
Array unit cell p^2 (μm²)

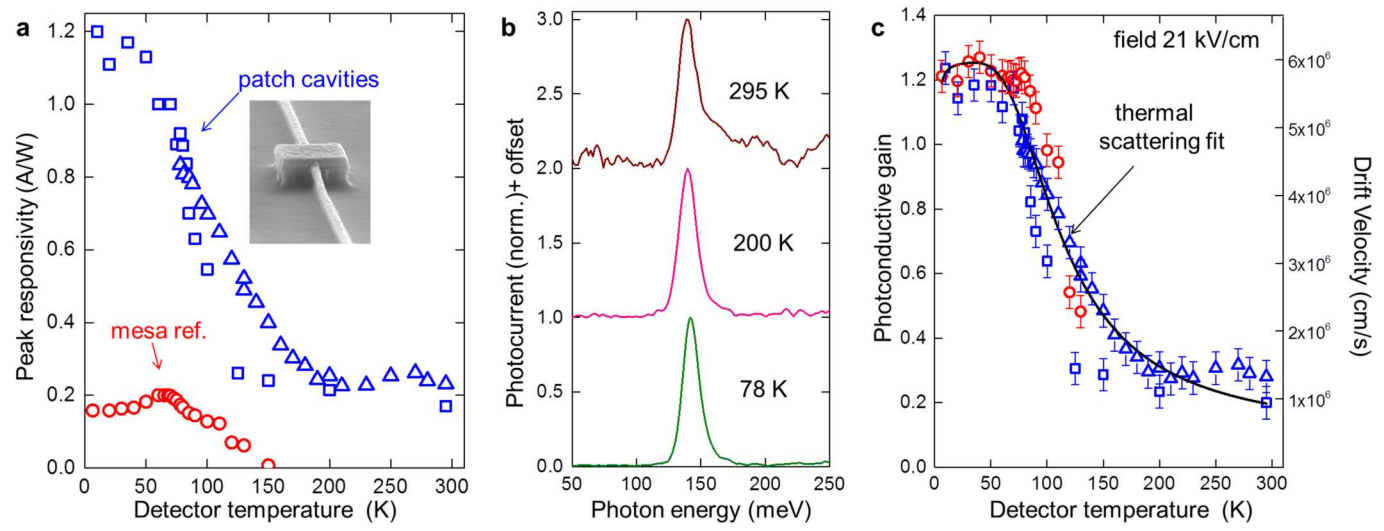
a
Peak responsivity (A/W)
Detector temperature (K)
patch cavities
mesa ref.
b
Photocurrent (norm.)+ offset
Photon energy (meV)
295 K
200 K
78 K
c
Photconductive gain
Drift Velocity (cm/s)
Detector temperature (K)
field 21 kV/cm
thermal
scattering fit

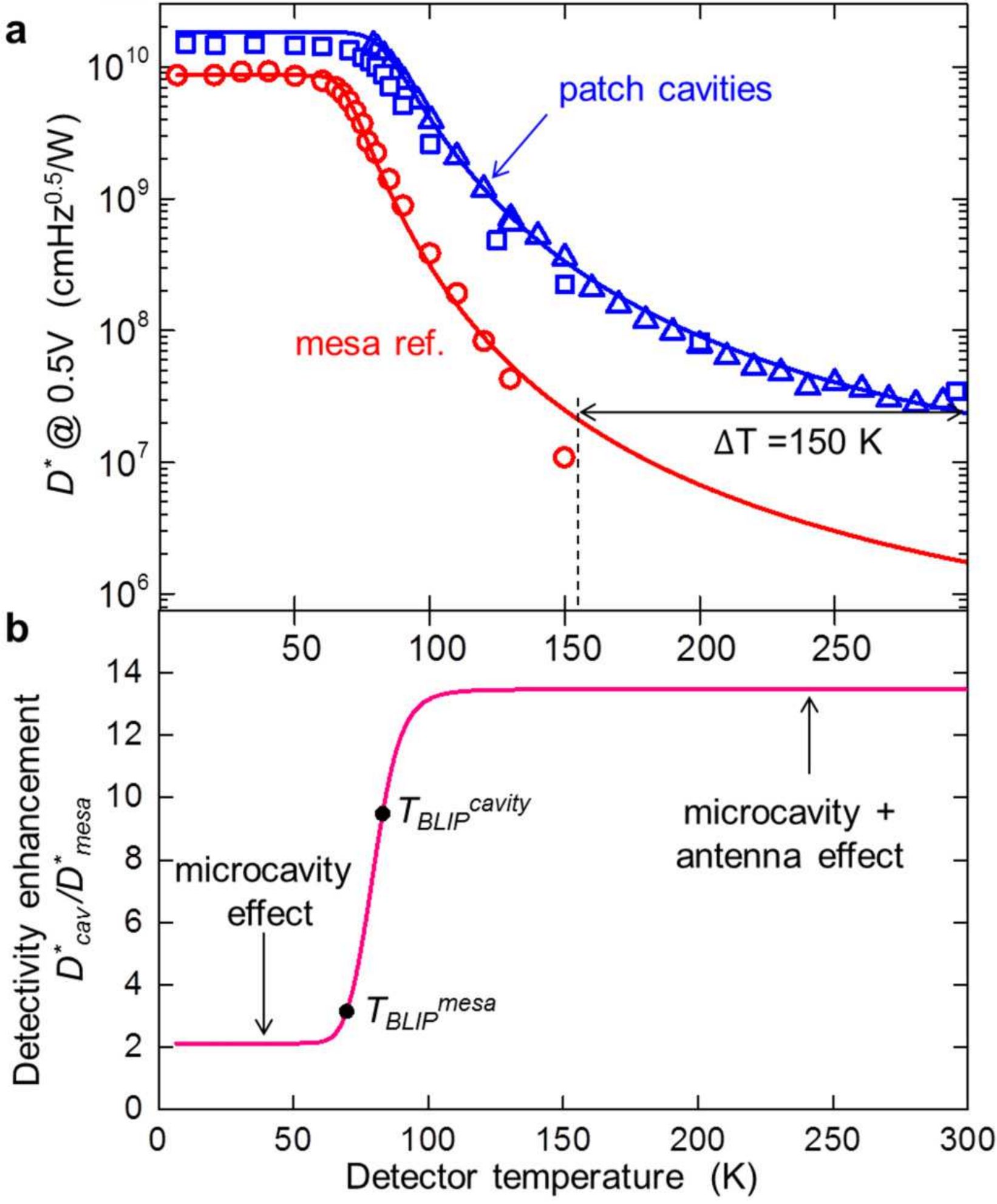
a
10^{10}
10^{9}
10^{8}
10^{7}
10^{6}
D^* @ 0.5V (cmHz$^{0.5}$/W)
patch cavities
mesa ref.
ΔT =150 K
50
100
150
200
250
b
14
12
10
8
6
4
2
0
Detectivity enhancement
D^*_{cav}/D^*_{mesa}
T_{BLIP}^{cavity}
T_{BLIP}^{mesa}
microcavity
effect
microcavity +
antenna effect
0
50
100
150
200
250
300
Detector temperature (K)

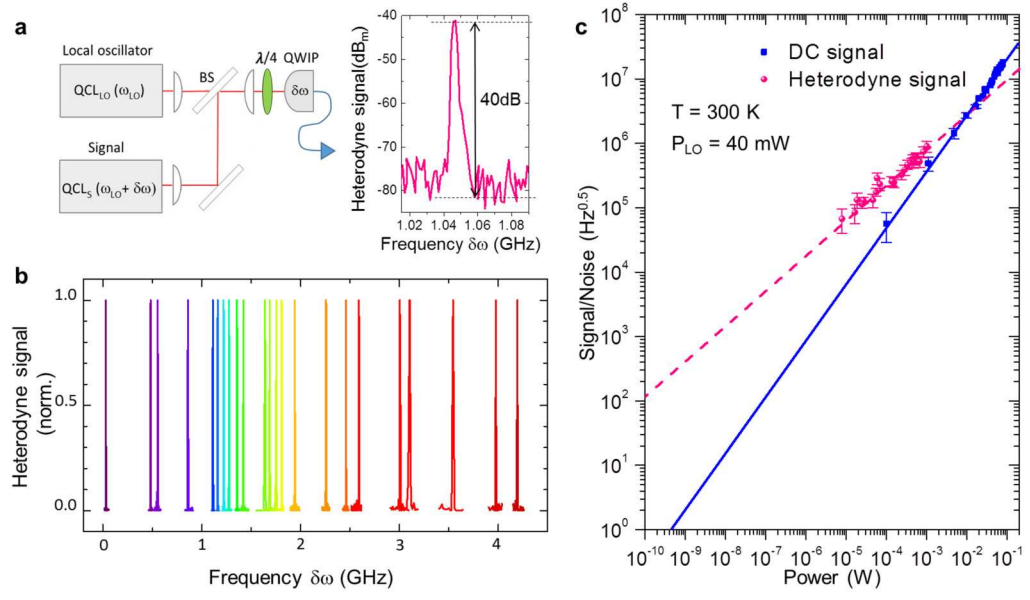
a
Local oscillator
QCL$_{LO}$ (ω_{LO})
BS
λ/4
QWIP
δω
Signal
QCL$_S$ (ω_{LO}+ δω)
Heterodyne signal(dBm)
40dB
Frequency δω (GHz)
b
Heterodyne signal (norm.)
Frequency δω (GHz)
c
DC signal
Heterodyne signal
T = 300 K
P_{LO} = 40 mW
Signal/Noise (Hz$^{0.5}$)
Power (W)